

Realization of high-fidelity perfect entangler between remote superconducting quantum processors

Juan Song^{1,2,3,*}, Shuang Yang^{1,*}, Pei Liu⁴, Guang-Ming Xue¹, Zhen-Yu Mi^{1,†}, Wen-Gang Zhang^{1,‡}, Fei Yan¹, Yi-Rong Jin¹, and Hai-Feng Yu^{1,5}

¹*Beijing Academy of Quantum Information Sciences, Beijing 100193, China*

²*Institute of Physics, Chinese Academy of Science, Beijing 100190, China*

³*University of Chinese Academy of Sciences, Beijing 101408, China*

⁴*State Key Laboratory of Low Dimensional Quantum Physics and Department of Physics, Tsinghua University, Beijing 100084, China and*

⁵*Hefei National Laboratory, Hefei 230088, China*

Building large-scale quantum computers from smaller modules offers a solution to many formidable scientific and engineering challenges. Nevertheless, engineering high-fidelity interconnects between modules remains challenging. In recent years, quantum state transfer (QST) has provided a way to establish entanglement between two separately packaged quantum devices. However, QST is not a unitary gate, thus cannot be directly inserted into a quantum circuit, which is widely used in recent quantum computation studies. Here we report a demonstration of a direct CNOT gate realized by the cross resonance (CR) effect between two remotely packaged quantum devices connected by a microwave cable. We achieve a CNOT gate with fidelity as high as $99.15 \pm 0.02\%$. The quality of the CNOT gate is verified by cross-entropy benchmarking (XEB) and further confirmed by demonstrating Bell-inequality violation. This work provides a new method to realize remote two-qubit gates. Our method can be used not only to achieve distributed quantum computing but also to enrich the topology of superconducting quantum chips with jumper lines connecting distant qubits. This advancement gives superconducting qubits broader application prospects in the fields of quantum computing and quantum simulation.

INTRODUCTION

Superconducting qubits represent one of the most promising hardware platforms for implementing quantum computation and quantum simulation [1–4]. Nevertheless, a significantly larger number of qubits is necessary for executing useful algorithms and achieving quantum error correction [5]. The certain size of chip limits the number of qubits on a superconducting quantum information processor, and the topological connectivity due to the planar graph also leads to an increase in the number of qubits or the depth of quantum circuit while implementing the quantum algorithm and quantum error correction which require high connectivity [6]. Thus, distributed quantum computation attracts wide attention, which offers a viable solution for scaling up quantum processors by connecting multiple small-scale quantum processors to facilitate large-scale quantum computation [7–10]. Recent studies on the quantum state transfer (QST) process have demonstrated that employing superconducting transmission lines to link small processors is a potential way for scaling up superconducting quantum computation [11–19]. However, the flying-photon-mediated QST process cannot be directly integrated into quantum circuits as it is not a unitary two-qubit gate.

Even the utilization of bi-directional flying photons to implement a SWAP gate does not result in a perfect entangler, thus precluding its use in forming a universal computation gate set [20]. Recent theoretical investigations have explored the cross resonance (CR) effect between two remotely connected quantum devices [21]. The CR gate applied on two fixed qubits is widely studied in recent quantum computation research. Its simplicity in implementation and insensitivity to flux noise show a great potential for scalable quantum computation with high fidelity [4, 22–36].

In this work, we present the realization of a direct CNOT gate between two separately packaged quantum devices via the CR effect. Unlike feedback-based protocols [37], our remote CNOT gate exhibits both high fidelity (99.15%) and low latency (gate time $< 200\text{ns}$). Compared to previous approaches [9], our superconducting cable method also enables the connection of qubits that are not nearest neighbors. Furthermore, by enriching the topological structure of 2D quantum chips, more efficient error correction codes become experimentally feasible. These advancements suggest that our results pave the way for future large-scale quantum computation.

RESULTS

The sample layout is shown in Figure 1. Our device consists of two modules, named Package A and Package B. Each package contains a single transmon qubit, the

* these authors contributed equally to this work

† mizy@baqis.ac.cn

‡ zhangwg@baqis.ac.cn

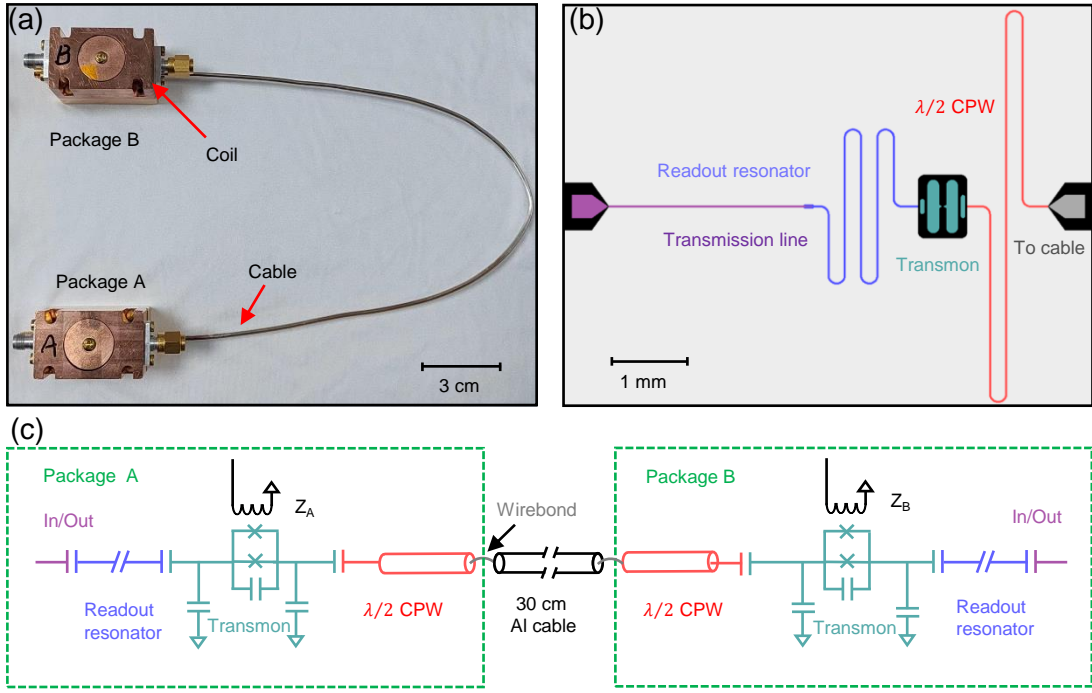


FIG. 1. Device description (a) Photograph of two packages. The packages are connected by 30-cm-long Al cable. Both cable ends are fixed to the sample boxes by solder. There is a coil on each of the copper sample box that can be applied with a current to tune the frequency of transmon qubit. (b) Micrograph of one chip compose of a transmission line (purple), frequency tunable transmon (turquoise), resonator (blue) and a half wavelength coplanar waveguide (red). (c) Circuit schematic of module A and module B

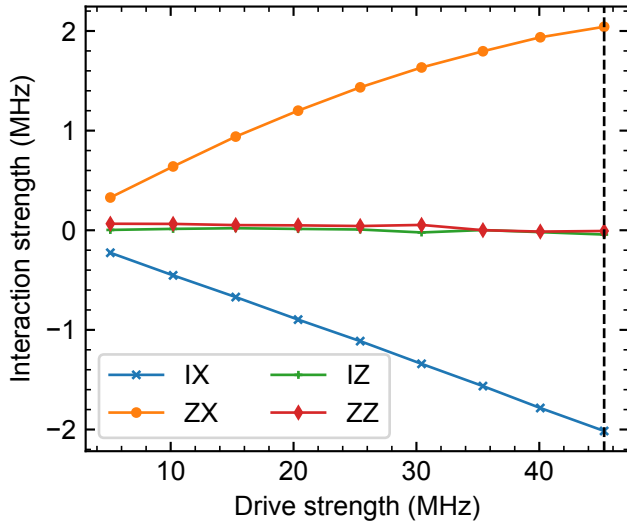


FIG. 2. CR parameters vs driving amplitude We use the Hamiltonian tomography method to get the CR parameters as a function of driving pulse amplitude. Dashed line indicates our actual working point.

frequency of which can be modulated by flux generated by the coil on the copper sample box. The transmon qubit is capacitively coupled to the readout resonator,

as well as a half-wavelength coplanar waveguide (CPW). The other end of the half-wavelength CPW is connected to an aluminum (Al) coaxial cable using superconducting Al wirebond. The bonding place is the node of the current standing wave. This design can reduce the losses caused by the wirebond. The two modules are connected by a 30-cm-long Al cable, with both ends fixed to the sample box by solder. Additional information regarding the sample fabrication process and experimental details can be found in the supplementary material.

The two quantum chip packages are mounted inside a μ -metal shield to reduce the impact of magnetic flux noise further. The entire system is then mounted on the 10mK cold plate of a dilution refrigerator (See Methods). We measure the 2D spectrum of both qubits. Several equidistant anti-crossing points indicate the interaction between the qubits and the standing mode of the transmission line. Here we emphasize that the Z-lines are used solely for determining the working point bias. We treat our qubits as frequency-fixed and do not apply any Z-pulses throughout the entire experiment.

The CR gate is one of the most widely employed gate to create an entanglement[4, 21]. For simplify, we write the effective two qubit CR drive Hamiltonian in terms of IX ,

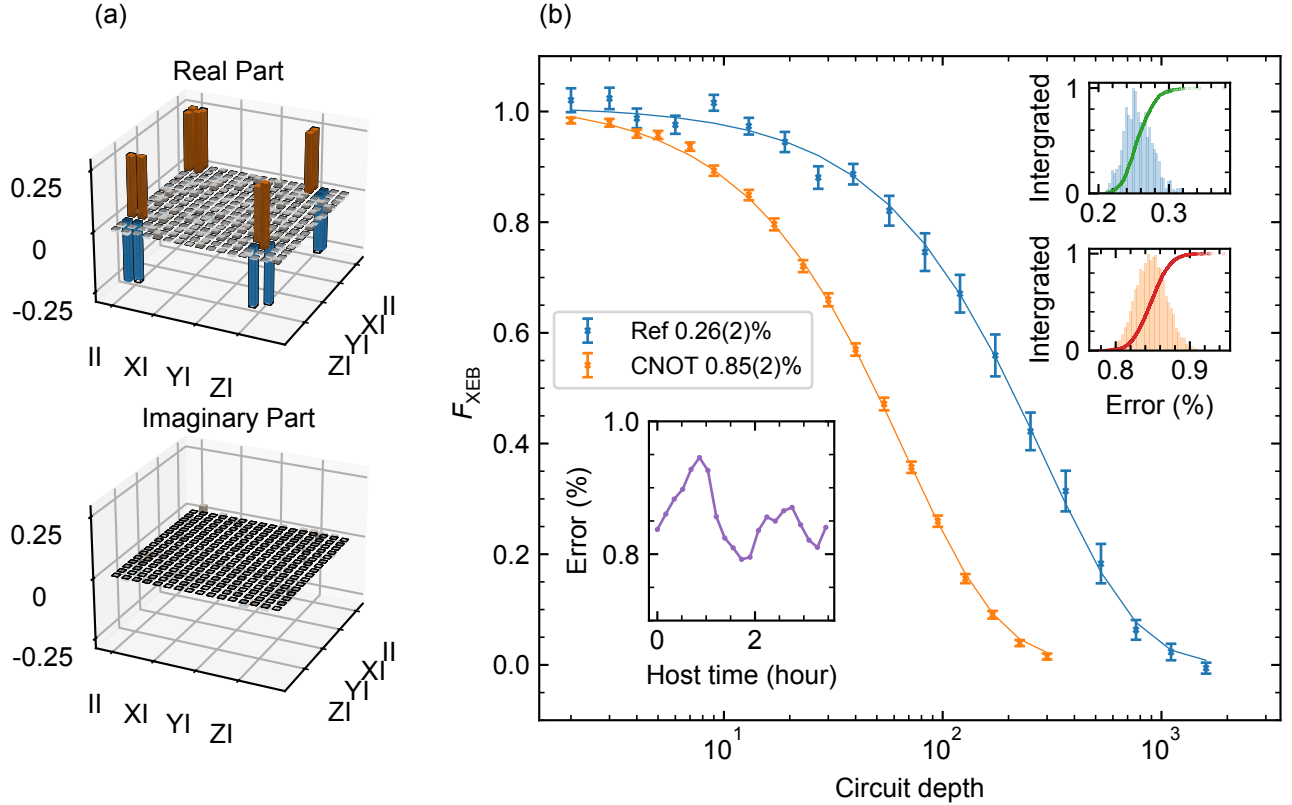


FIG. 3. **Quantum process tomography and cross-entropy benchmarking** (a) The real part and imaginary part of the quantum process matrix. The process fidelity is measured to be $F = 98.89\%$. (b) XEB Fidelity vs circuit depth. The orange dots are the result of interleaved circuit for CNOT gate XEB. The blue dots are the result of single-bit gate only circuit which is used for reference. The right insets show the histogram of gate fidelity distribution. The left inset shows the monitor of the time-stability.

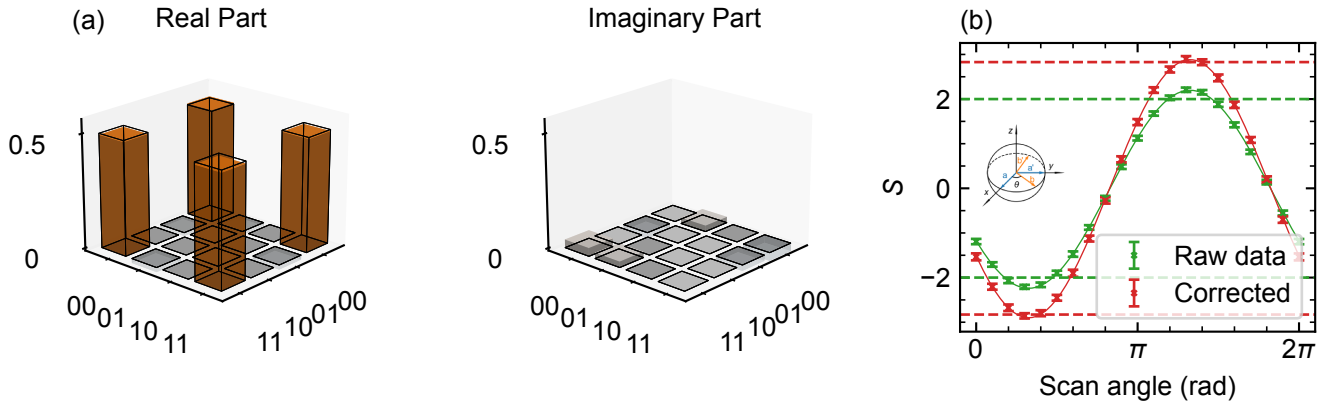


FIG. 4. **Bell state preparation and Bell inequality measurement** (a) The real part and imaginary part of the Bell state density matrix. The state fidelity is measured to be $F = 99.14\%$. (b) The CHSH correlation vs scan angle. The green dots indicate the data without readout correction while the red dots indicate the data with readout correction. Classical and quantum limits are marked with horizontal dashed lines.

IY , IZ , ZX , ZY , and ZZ (See Methods):

$$H_{\text{eff}} = \omega_{IX}I \otimes X + \omega_{IY}I \otimes Y + \omega_{IZ}I \otimes Z + \omega_{ZX}Z \otimes X + \omega_{ZY}Z \otimes Y + \omega_{ZZ}Z \otimes Z, \quad (1)$$

where X, Y and Z are the Pauli matrices. Using the method in Ref [38], we perform the CR Rabi experiments while the control bit is on its $|0\rangle$ and $|1\rangle$ state respectively. On each control qubit state, we vary the driving time and use the quantum state tomography to get the final state Bloch vector $(X_{|0\rangle,|1\rangle}, Y_{|0\rangle,|1\rangle}, Z_{|0\rangle,|1\rangle})$. By fitting the result data with the Bloch equation model, we can extract the six parameters. Then, we vary the driving amplitude and get these Hamiltonian parameters as a function of driving amplitude (See Fig 2).

Based on these results, we can now calibrate our direct CNOT gate. To be more specific, our ultimate goal is to realize a two-qubit gate that the target qubit stays at the initial state (or rotates along X-axis by an angle of π) when the control qubit is on its $|0\rangle$ (or $|1\rangle$) state. Firstly, we scan the CR pulse phase to find the phase at which the ZX component is maximized while the ZY component is zero. Then, for rough calibration, we scan the amplitude and phase of the target active cancellation pulse to minimize the excitation on the target qubit when the control qubit is on $|0\rangle$.

Next, we apply a circuit-based calibration sequence for fine calibration. To achieve a high fidelity CNOT gate, we use the DRAG method [39, 40] to suppress the off-resonance driving induced excitation on the control qubit and drive-induced AC stark shift on the target qubit. During the fine calibration procedure, we apply an array of CNOT gates to amplify the error and thus find the best pulse parameters. So far, the gate is tuned to be $|0\rangle\langle 0| \otimes I + e^{i\varphi}|1\rangle\langle 1| \otimes X$. Finally, we cancel the drive-induced phase φ with control qubit frame change and bring the gate to a standard CNOT. (See Methods) To evaluate the performance of the calibrated CNOT gate, we utilize two different methods: quantum process tomography (QPT) and cross-entropy benchmarking (XEB). With the QPT method, the process matrix χ is obtained and compared to the ideal matrix χ_{ideal} . The process fidelity is measured to be $F_p = \text{Tr}(\chi \cdot \chi_{\text{ideal}}) = 98.89\%$. However, the state preparation and measurement (SPAM) error is not ruled out in QPT experiment. Thus, we implement the XEB benchmarking method which is able to estimate the process fidelity independently of the SPAM error[41]. By fitting the decay rate of XEB fidelity Vs the number of CNOT gates, the average fidelity of our CNOT gate is estimated to be $(99.15 \pm 0.02)\%$ (See Methods).

Finally, we show the ability to establish a remote entanglement between the two packages: we first apply a Hadamard gate on the control qubit. Then, a CNOT gate prepares the system onto one of the Bell states $|\Phi^+\rangle = (|00\rangle + |11\rangle)/\sqrt{2}$. We reconstruct the density matrix of our prepared state and compare it with the

ideal state density matrix. The state fidelity is measured to be 99.14%.

We also perform the Clauser–Horne–Shimony–Holt (CHSH) Bell inequality test on our remotely entangled state. The control qubit is measured along $a = x$ or $a_\perp = y$. Simultaneously, the target qubit is measured along b or b_\perp . The angle between a and b is scanned. Without readout correction, the maximum CHSH correlation $S = 2.208 \pm 0.050$, which exceeds the maximum classical value 2 by 4.2 standard deviations. After readout correction, the maximum correlation $S = 2.898 \pm 0.064$. The correlation is a little bit higher than the quantum limit $2\sqrt{2}$. This error mainly comes from the thermal excitation on two qubits.

CONCLUSION

In conclusion, we present the realization of a direct CNOT gate between two separately packaged quantum chips. The average fidelity of 99.15 ± 0.02 is characterized through the XEB method. Our method does not require any post-selection or feedback thus it is high efficient and low latency. These advancements mark a significant step towards scalable quantum computing, providing a robust foundation for developing sophisticated quantum algorithms and error correction techniques necessary for practical and large-scale quantum systems.

Note added — We noticed another work on realizing remote two-qubit gate on superconducting quantum devices recently[42].

- [1] F. Arute, K. Arya, R. Babbush, D. Bacon, J. C. Bardin, R. Barends, R. Biswas, S. Boixo, F. G. Brandao, D. A. Buell, *et al.*, Quantum supremacy using a programmable superconducting processor, *Nature* **574**, 505 (2019).
- [2] X. Zhang, W. Jiang, J. Deng, K. Wang, J. Chen, P. Zhang, W. Ren, H. Dong, S. Xu, Y. Gao, *et al.*, Digital quantum simulation of floquet symmetry-protected topological phases, *Nature* **607**, 468 (2022).
- [3] G. Q. Ai, Suppressing quantum errors by scaling a surface code logical qubit, *Nature* **614**, 676 (2023).
- [4] P. Jurcevic, A. Javadi-Abhari, L. S. Bishop, I. Lauer, D. F. Bogorin, M. Brink, L. Capelluto, O. Günlük, T. Itoko, N. Kanazawa, *et al.*, Demonstration of quantum volume 64 on a superconducting quantum computing system, *Quantum Sci. Technol.* **6**, 025020 (2021).
- [5] A. G. Fowler, M. Mariantoni, J. M. Martinis, and A. N. Cleland, Surface codes: Towards practical large-scale quantum computation, *Phys. Rev. A* **86**, 032324 (2012).
- [6] S. Bravyi, A. W. Cross, J. M. Gambetta, D. Maslov, P. Rall, and T. J. Yoder, High-threshold and low-overhead fault-tolerant quantum memory, *Nature* **627**, 778 (2024).

[7] L. Jiang, J. M. Taylor, A. S. Sørensen, and M. D. Lukin, Distributed quantum computation based on small quantum registers, *Phys. Rev. A* **76**, 062323 (2007).

[8] C. Monroe, R. Raussendorf, A. Ruthven, K. R. Brown, P. Maunz, L.-M. Duan, and J. Kim, Large-scale modular quantum-computer architecture with atomic memory and photonic interconnects, *Phys. Rev. A* **89**, 022317 (2014).

[9] A. Gold, J. Paquette, A. Stockklauser, M. J. Reagor, M. S. Alam, A. Bestwick, N. Didier, A. Nersisyan, F. Oruc, A. Razavi, *et al.*, Entanglement across separate silicon dies in a modular superconducting qubit device, *npj Quantum Inf.* **7**, 142 (2021).

[10] J. Ang, G. Carini, Y. Chen, I. Chuang, M. DeMarco, S. Economou, A. Eickbusch, A. Faraon, K.-M. Fu, S. Girvin, *et al.*, Arquin: architectures for multinode superconducting quantum computers, *ACM Trans. Quantum Comput.*.

[11] N. Leung, Y. Lu, S. Chakram, R. Naik, N. Ernest, R. Ma, K. Jacobs, A. Cleland, and D. Schuster, Deterministic bidirectional communication and remote entanglement generation between superconducting qubits, *npj Quantum Inf.* **5**, 18 (2019).

[12] Y. Zhong, H.-S. Chang, K. Satzinger, M.-H. Chou, A. Bienfait, C. Conner, É. Dumur, J. Grebel, G. Peairs, R. Povey, *et al.*, Violating bell's inequality with remotely connected superconducting qubits, *Nat. Phys.* **15**, 741 (2019).

[13] P. Magnard, S. Storz, P. Kurpiers, J. Schär, F. Marxer, J. Lütolf, T. Walter, J.-C. Besse, M. Gabureac, K. Reuer, *et al.*, Microwave quantum link between superconducting circuits housed in spatially separated cryogenic systems, *Phys. Rev. Lett.* **125**, 260502 (2020).

[14] P. Campagne-Ibarcq, E. Zalys-Geller, A. Narla, S. Shankar, P. Reinhold, L. Burkhardt, C. Axline, W. Pfaff, L. Frunzio, R. J. Schoelkopf, and M. H. Devoret, Deterministic remote entanglement of superconducting circuits through microwave two-photon transitions, *Phys. Rev. Lett.* **120**, 200501 (2018).

[15] Y. Zhong, H.-S. Chang, A. Bienfait, É. Dumur, M.-H. Chou, C. R. Conner, J. Grebel, R. G. Povey, H. Yan, D. I. Schuster, *et al.*, Deterministic multi-qubit entanglement in a quantum network, *Nature* **590**, 571 (2021).

[16] H. Yan, Y. Zhong, H.-S. Chang, A. Bienfait, M.-H. Chou, C. R. Conner, É. Dumur, J. Grebel, R. G. Povey, and A. N. Cleland, Entanglement purification and protection in a superconducting quantum network, *Phys. Rev. Lett.* **128**, 080504 (2022).

[17] S. Storz, J. Schär, A. Kulikov, P. Magnard, P. Kurpiers, J. Lütolf, T. Walter, A. Copetudo, K. Reuer, A. Akin, *et al.*, Loophole-free bell inequality violation with superconducting circuits, *Nature* **617**, 265 (2023).

[18] H.-S. Chang, Y. P. Zhong, A. Bienfait, M.-H. Chou, C. R. Conner, E. Dumur, J. Grebel, G. A. Peairs, R. G. Povey, K. J. Satzinger, and A. N. Cleland, Remote entanglement via adiabatic passage using a tunably dissipative quantum communication system, *Phys. Rev. Lett.* **124**, 240502 (2020).

[19] J. Niu, L. Zhang, Y. Liu, J. Qiu, W. Huang, J. Huang, H. Jia, J. Liu, Z. Tao, W. Wei, *et al.*, Low-loss interconnects for modular superconducting quantum processors, *Nat. Electron.* **6**, 235 (2023).

[20] J. Zhang, J. Vala, S. Sastry, and K. B. Whaley, Geometric theory of nonlocal two-qubit operations, *Phys. Rev. A* **67**, 042313 (2003).

[21] M. Ohfuchi and S. Sato, Remote cross-resonance gate between superconducting fixed-frequency qubits, *Quantum Sci. Technol.* **9**, 035014 (2024).

[22] P. de Groot, J. Lisenfeld, R. Schouten, S. Ashhab, A. Lupaşcu, C. Harmans, and J. Mooij, Selective darkening of degenerate transitions demonstrated with two superconducting quantum bits, *Nat. Phys.* **6**, 763 (2010).

[23] C. Rigetti and M. Devoret, Fully microwave-tunable universal gates in superconducting qubits with linear couplings and fixed transition frequencies, *Phys. Rev. B* **81**, 134507 (2010).

[24] J. M. Chow, A. D. Córcoles, J. M. Gambetta, C. Rigetti, B. R. Johnson, J. A. Smolin, J. R. Rozen, G. A. Keefe, M. B. Rothwell, M. B. Ketchen, *et al.*, Simple all-microwave entangling gate for fixed-frequency superconducting qubits, *Phys. Rev. Lett.* **107**, 080502 (2011).

[25] P. de Groot, S. Ashhab, A. Lupaşcu, L. DiCarlo, F. Nori, C. Harmans, and J. Mooij, Selective darkening of degenerate transitions for implementing quantum controlled-not gates, *New J. Phys.* **14**, 073038 (2012).

[26] A. D. Córcoles, J. M. Gambetta, J. M. Chow, J. A. Smolin, M. Ware, J. Strand, B. L. Plourde, and M. Steffen, Process verification of two-qubit quantum gates by randomized benchmarking, *Phys. Rev. A* **87**, 030301 (2013).

[27] A. Patterson, J. Rahamim, T. Tsunoda, P. Spring, S. Jebari, K. Ratter, M. Mergenthaler, G. Tancredi, B. Vlastakis, M. Esposito, *et al.*, Calibration of a cross-resonance two-qubit gate between directly coupled transmons, *Phys. Rev. Appl.* **12**, 064013 (2019).

[28] V. Tripathi, M. Khezri, and A. N. Korotkov, Operation and intrinsic error budget of a two-qubit cross-resonance gate, *Phys. Rev. A* **100**, 012301 (2019).

[29] M. Ware, B. Johnson, J. Gambetta, T. Ohki, J. Chow, and B. Plourde, Cross-resonance interactions between superconducting qubits with variable detuning, Preprint at <https://arxiv.org/abs/1905.11480>.

[30] J. Ku, X. Xu, M. Brink, D. C. McKay, J. B. Hertzberg, M. H. Ansari, and B. Plourde, Suppression of unwanted zz interactions in a hybrid two-qubit system, *Phys. Rev. Lett.* **125**, 200504 (2020).

[31] A. Kandala, K. X. Wei, S. Srinivasan, E. Magesan, S. Carnevale, G. Keefe, D. Klaus, O. Dial, and D. McKay, Demonstration of a high-fidelity cnot gate for fixed-frequency transmons with engineered zz suppression, *Phys. Rev. Lett.* **127**, 130501 (2021).

[32] M. Malekakhlagh, E. Magesan, and D. C. McKay, First-principles analysis of cross-resonance gate operation, *Phys. Rev. A* **102**, 042605 (2020).

[33] E. Magesan and J. M. Gambetta, Effective hamiltonian models of the cross-resonance gate, *Phys. Rev. A* **101**, 052308 (2020).

[34] B. K. Mitchell, R. K. Naik, A. Morvan, A. Hashim, J. M. Kreikebaum, B. Marinelli, W. Lavrijsen, K. Nowrouzi, D. I. Santiago, and I. Siddiqi, Hardware-efficient microwave-activated tunable coupling between superconducting qubits, *Phys. Rev. Lett.* **127**, 200502 (2021).

[35] K. Wei, E. Magesan, I. Lauer, S. Srinivasan, D. Bogorin, S. Carnevale, G. Keefe, Y. Kim, D. Klaus, W. Landers, *et al.*, Quantum crosstalk cancellation for fast entangling gates and improved multi-qubit performance, Preprint at <https://arxiv.org/abs/2106.00675> (2021).

[36] X. Xu and M. Ansari, Zz freedom in two-qubit gates, *Phys. Rev. Appl.* **15**, 064074 (2021).

[37] J. Qiu, Y. Liu, J. Niu, L. Hu, Y. Wu, L. Zhang, W. Huang, Y. Chen, J. Li, S. Liu, *et al.*, Deterministic quantum teleportation between distant superconducting chips, Preprint at <https://arxiv.org/abs/2302.08756> (2023).

[38] S. Sheldon, E. Magesan, J. M. Chow, and J. M. Gambetta, Procedure for systematically tuning up cross-talk in the cross-resonance gate, *Phys. Rev. A* **93**, 060302 (2016).

[39] Z. Chen, J. Kelly, C. Quintana, R. Barends, B. Campbell, Y. Chen, B. Chiaro, A. Dunsworth, A. Fowler, E. Lucero, *et al.*, Measuring and suppressing quantum state leakage in a superconducting qubit, *Phys. Rev. Lett.* **116**, 020501 (2016).

[40] J. M. Gambetta, F. Motzoi, S. Merkel, and F. K. Wilhelm, Analytic control methods for high-fidelity unitary operations in a weakly nonlinear oscillator, *Phys. Rev. A* **83**, 012308 (2011).

[41] C. Neill, P. Roushan, K. Kechedzhi, S. Boixo, S. V. Isakov, V. Smelyanskiy, A. Megrant, B. Chiaro, A. Dunsworth, K. Arya, *et al.*, A blueprint for demonstrating quantum supremacy with superconducting qubits, *Science* **360**, 195 (2018).

[42] M. Mollenhauer, A. Irfan, X. Cao, S. Mandal, and W. Pfaff, A high-efficiency plug-and-play superconducting qubit network, Preprint at <https://arxiv.org/abs/2407.16743> (2024).

ACKNOWLEDGEMENTS

We thank Dr. He Wang and Dr. Kehuan Linghu for their helpful discussions. We acknowledge supports from the National Natural Science Foundation of China (Grant Nos. 92365206,12322413), Innovation Program for Quantum Science and Technology (No.2021ZD0301802).

METHODS

Sample fabrication

The base circuit, comprising a transmon qubit, transmission line, readout resonator, and a half-wavelength coplanar waveguide, along with the Josephson junction, is fabricated on a single-sided polished sapphire substrate. The fabrication process unfolds with the following sequence of steps:

1. The substrate undergoes annealing in atmosphere for 3 hours at 1200°C, following a 200nm layer of alpha-phase Ta film deposition as the base layer.
2. Photolithography patterns the base circuit using a laser direct writing system (DWL 66+), and CF4 reactive ion etching is employed for dry etching.
3. The photoresist is subsequently removed, and the sample is immersed in a piranha solution (H₂SO₄ and H₂O₂ with a ratio of 2:1) for 20 minutes to eliminate

residual photoresist and to induce strong oxidation on the Ta film's surface.

4. Utilizing electron beam lithography with a bilayer of photoresists (PMMA A4/LOR 10B), the Josephson junction patterns are precisely exposed.
5. The Josephson junction is then deposited through a double-angle evaporation within a E-beam evaporator, preceded thorough surface cleaning via ion beam milling.
6. Once the wafer is segmented into individual chips, the lift-off process is executed in N-Methylpyrrolidone, which removes the PMMA A4/LOR 10B resist and Al film from the sample surface, leaving the Josephson junction. The sample is subsequently wire-bonded to a copper sample box using a superconducting Al wire.

Connection between chip and cable

In this experiment, two 7mm×7mm chips are fabricated on a single-sided polished sapphire substrate and placed within two copper sample boxes, respectively. The ground of the chip is connected to the copper sample box with superconducting Al wirebonds (See Fig 5). The two modules are connected using a 30-cm-long Al coaxial cable with outer and inner conductor diameters of 2.2mm and 0.86mm, respectively. The cable is fixed to the sample box by solder. The half-wavelength coplanar waveguide (CPW) is connected to an Al coaxial cable via 50 – μ m diameter superconducting Al wirebonds. The outer conductors and the dielectric material at both ends of the cable are removed to expose the inner conductors for wire bonding, as displayed in Fig 5(b). The half-wavelength CPW is open and capacitively coupled to the transmon qubit, so both ends of the half-wavelength CPW are current wave nodes. Although this design can mitigate the losses associated with wire bonds, the length of the wirebonds should be minimized. Furthermore, the utilization of multiple bonding wires between the cable and the half-wavelength CPW can not only circumvent the potential damage caused by the sample installation process, but also reduce the loss result from the wirebond joint.

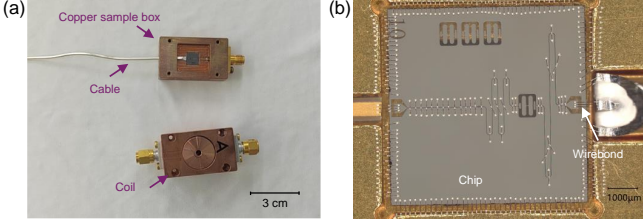


FIG. 5. (a). Image of the device consisting of a copper sample box, chip, Al coaxial cable and coil. (b) Photograph of a quantum module, showing transmission line, Transmon qubit, readout resonator and half-wavelength coplanar waveguide circuitries.

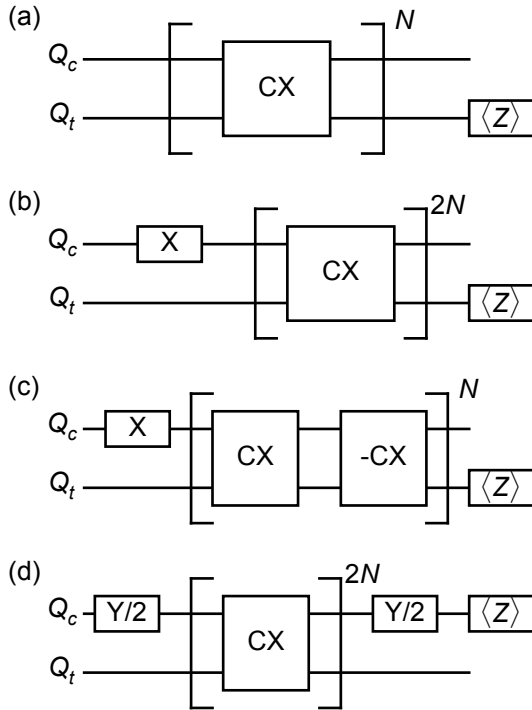


FIG. 6. The circuits used for fine CNOT gate calibration.

System Hamiltonian

The full CR Hamiltonian of our system can be written as:

$$\begin{aligned}
 H_{\text{sys}} = & \omega_c Z_c + \Omega_c \cos(\omega_t t + \phi_c) X_c \\
 & + \omega_t Z_t + \Omega_t \cos(\omega_t t + \phi) X_t \\
 & + \sum_n [\omega_n a_n^\dagger a_n + g_{c,n}(a^\dagger + a) \otimes X_c \\
 & \quad + (-1)^n g_{t,n}(a^\dagger + a) \otimes X_t] \\
 & + \sum_n [\alpha_{n,c} \Omega_c \cos(\omega_t t + \phi_c) \\
 & \quad \alpha_{n,t} \Omega_t \cos(\omega_t t + \phi_t) (a_n^\dagger + a_n)]
 \end{aligned}$$

where c and t denote the control and target qubit, n denotes the n th mode of the cable, $g_{c,n}$ ($g_{t,n}$) denotes the coupling between the control (target) qubit and the n th mode of the cable and $\alpha_{c,n}$ ($\alpha_{t,n}$) denotes the control (target) qubit drive signal's leakage rate onto the n th mode of the cable. Actually, the leakage terms will cause extra CR effect on the target qubit (here, "control qubits" are the cavity modes).

Here we study our system in the sub-space of the control and target qubit only. The coupling terms result a direct qubit-qubit coupling. In our experiment, we never excite the cable mode. Thus the leakage terms can all be absorbed into the IX and IY term. Finally, by applying a unitary transformation $U = \exp[-i(\omega_t t Z_c + \omega_t t Z_t)/2]$ and the rotating wave approximation (RWA), we achieve the effective Hamiltonian:

$$\begin{aligned}
 H_{\text{eff}} = & \omega_{IX} I \otimes X + \omega_{IY} I \otimes Y + \omega_{IZ} I \otimes Z \\
 & + \omega_{ZX} Z \otimes X + \omega_{ZY} Z \otimes Y + \omega_{ZZ} Z \otimes Z
 \end{aligned}$$

Gate Calibration Method

We calibrate the CNOT gate with the circuits shown in Fig S2. Circuit (a) is used for calibrate the amplitude and phase of the cancellation pulse. Circuit (b) and (c) are used for calibrate the amplitude and the DRAG parameter of the CR drive. Circuit (d) is used for control qubit frame changing calibration.

XEB data

We use the XEB method mentioned in [26] to verify the fidelity of our single-bit gate and CNOT gate fidelity. For single-bit case, on each layer, we randomly choose a gate from $U(\theta) = \exp[-i\pi(X \cos \theta + Y \sin \theta)/4]$, where $\theta = 0, \pi/4, 2\pi/4, \dots, 7\pi/4$. We fit the decay curve of cross-entropy benchmarking fidelity with exponential function to get p_{ref} , the average fidelity of the single-bit gate layer.

Then, we interleave the CNOT gate into each layer and get the fidelity p_{int} . Finally, we calculate the CNOT gate fidelity with $F_{\text{CNOT}} = 1 - (D-1)(1 - p_{\text{int}}/p_{\text{ref}})/D$, where D is the system dimension (here, $D = 4$).

For CNOT case, we take the data from 500 different measurements which lasts for 3.75 hours. Then, we use the bootstrap resampling method to resample the data for 10000 times to calculate the deviation of the fidelity. We also choose different time window to calculate the time-stability of the gate fidelity. (See Main Text)